Evidence of the Topological Hall Effect in Pt/Antiferromagnetic Insulator Bilayers

Yang Cheng,[1,*] Sisheng Yu,[1,*] Menglin Zhu,[2] Jinwoo Hwang,[2] and Fengyuan Yang[1]
[1]*Department of Physics, The Ohio State University, Columbus, Ohio 43210, USA*
[2]*Department of Materials Science and Engineering, The Ohio State University, Columbus, Ohio 43212, USA*

(Received 20 May 2019; revised manuscript received 4 November 2019; published 5 December 2019)

The topological Hall effect has been a primary indicator of nontrivial spin textures in magnetic materials. We observe the evidence of the topological Hall effect in Pt/Cr_2O_3 bilayers grown on $Al_2O_3(0001)$ and $Al_2O_3(11\bar{2}0)$, where the Cr_2O_3 epitaxial film is an antiferromagnetic insulator. The Pt/Cr_2O_3 bilayers exhibit topological Hall resistivity for Cr_2O_3 thicknesses below 6 nm near and above room temperature, which is above the Néel temperature of Cr_2O_3, revealing the key role of thermal fluctuations in the formation of spin textures. The similarity of topological Hall signals in (0001)- and $(11\bar{2}0)$-oriented Cr_2O_3 films indicates that the emergence of spin textures is insensitive to crystalline orientation.

DOI: 10.1103/PhysRevLett.123.237206

Topological spin textures, such as skyrmions, have attracted intense interest in recent years [1–8]. The competition between exchange interaction, magnetic anisotropy, and Dzyaloshinskii-Moriya interaction (DMI) generates chiral spin textures in bulk noncentrosymmetric materials [9] and magnetic multilayers [10]. Electric transport measurement via the topological Hall (TH) effect is a powerful tool for detecting spin textures. In conducting skyrmion materials, the TH effect arises when electrons flowing in the spin textures experience an emergent electromagnetic field through interaction with the textured spins [1] and are scattered off of the textures, producing a uniquely identifiable TH voltage [11].

Magnetic skyrmions have been studied almost exclusively in bulk ferromagnets (FM) or FM multilayers. Antiferromagnets (AF) [12–14] have also been predicted to harbor topological spin textures such as AF skyrmions [15–17]. To date, except some noncollinear AFs with intrinsic chirality [18], only a few experiments have included AFs in their heterostructures to show spin chirality [19,20], where the AFs solely play an auxiliary role, such as providing an exchange bias [19] or an AF heavy metal (HM) to generate a large interfacial DMI [20] while spin chirality emerges in the neighboring layer. Recently, thermally driven spin chirality fluctuations have been predicted in materials with spin frustrations [21,22] and verified in 2D Ising FMs [23] even above their Curie temperatures (T_C). Here, we report the detection of topological spin textures in Pt/Cr_2O_3 bilayers using the TH effect near and above the Néel temperature (T_N) of AF insulator (AFI) Cr_2O_3 films.

Epitaxial Cr_2O_3 thin films are grown on $Al_2O_3(0001)$ and $Al_2O_3(11\bar{2}0)$ substrates using off-axis sputtering at a substrate temperature of 500 °C [24–27]. Figure 1(a) shows $2\theta/\omega$ x-ray diffraction (XRD) scans for Cr_2O_3 (30 nm) films on $Al_2O_3(0001)$ and $Al_2O_3(11\bar{2}0)$. Figure 1(b) shows an XRD rocking curve of the Cr_2O_3 (0006) peak for the (0001)-oriented film [the $(11\bar{2}0)$-oriented film gives a similar rocking curve]. The clear Laue oscillations and narrow full-width-at-half-maximum (FWHM) of the rocking curves indicate the high crystal quality of the Cr_2O_3 films in both orientations. Figure 1(c) shows an x-ray reflectometry (XRR) scan of the Cr_2O_3 film on $Al_2O_3(0001)$, where the fitting gives a roughness of 0.1 nm. The smooth surface is confirmed by atomic force microscopy (AFM) as shown in Fig. 1(d) with a roughness of 0.1 nm. The scanning transmission electron microscopy image for a 30 nm Cr_2O_3 film on $Al_2O_3(0001)$ in Fig. 1(e) reveals the epitaxy and single crystal ordering of Cr_2O_3.

Given that Cr_2O_3 is insulating, the predicted topological spin textures in the AF, if they exist, cannot be directly detected electrically. We deposit a 2 nm Pt layer on Cr_2O_3 films of various thicknesses (t) at room temperature using off-axis sputtering, where the Pt layer provides a channel for Hall measurement as well as interfacial DMI needed for the formation of spin textures. The Pt(2 nm)/$Cr_2O_3(t)$ bilayers are patterned into Hall bars with a current channel width of 100 μm.

Figure 2(a) shows the Hall resistivity for a Pt(2 nm)/Cr_2O_3(5 nm) bilayer on $Al_2O_3(0001)$ at a temperature (T) of 345 K with an out-of-plane field ($\boldsymbol{H}$) and a dc current of 100 μA. In general, there are three terms in the Hall resistivity, $\rho_{xy} = \rho_{OH} + \rho_{AH} + \rho_{TH}$, including the ordinary Hall (ρ_{OH}), anomalous Hall (ρ_{AH}), and topological Hall (ρ_{TH}) resistivities [7,28]. ρ_{OH} has a linear field dependence. At 345 K, ρ_{AH} in the Pt/Cr_2O_3 bilayer is due to the spin Hall anomalous Hall effect (SH AHE) [29,30]. Since 345 K is higher than the $T_N = 307$ K [31] of bulk Cr_2O_3 and ~280 K for 20 nm $Cr_2O_3(0001)$ [32], we use the Langevin function to fit the SH AHE data as shown in Fig. 2(a), which agrees well with the experimental data at $|H| < 0.2$ T and $|H| > 1.4$ T. However, there is a pronounced

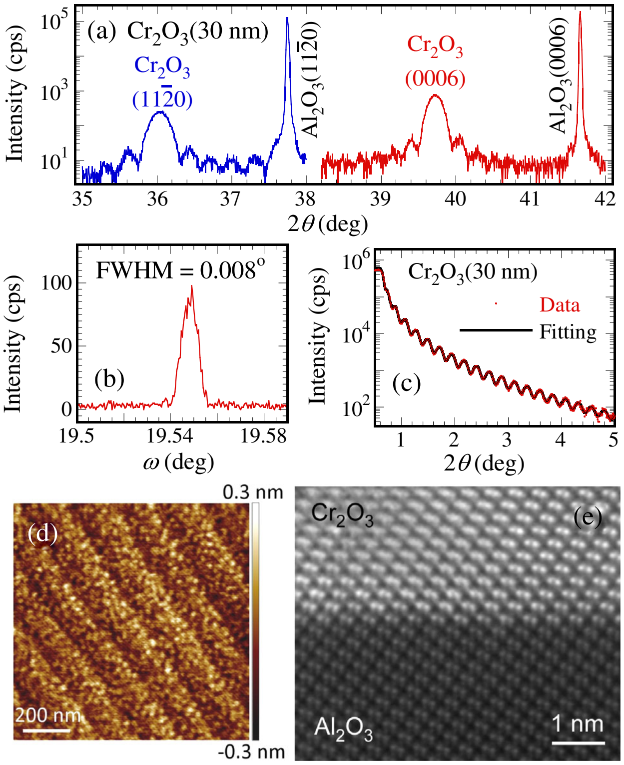

FIG. 1. (a) $2\theta/\omega$ XRD scans of a 30 nm Cr_2O_3 epitaxial film grown on Al_2O_3 (0001) and Al_2O_3 $(11\bar{2}0)$ substrates. (b) XRD rocking curve of the Cr_2O_3 (0006) peak for the film on Al_2O_3 (0001). (c) XRR scan of a 30 nm Cr_2O_3 film on Al_2O_3 (0001), where the fitting (black curve) gives a Cr_2O_3 thickness of 30 nm and a roughness of 0.1 nm. (d) AFM image of a 30 nm Cr_2O_3 film on Al_2O_3 (0001) with a surface roughness of 0.1 nm. (d) STEM image of a 30 nm Cr_2O_3 film on Al_2O_3 (0001).

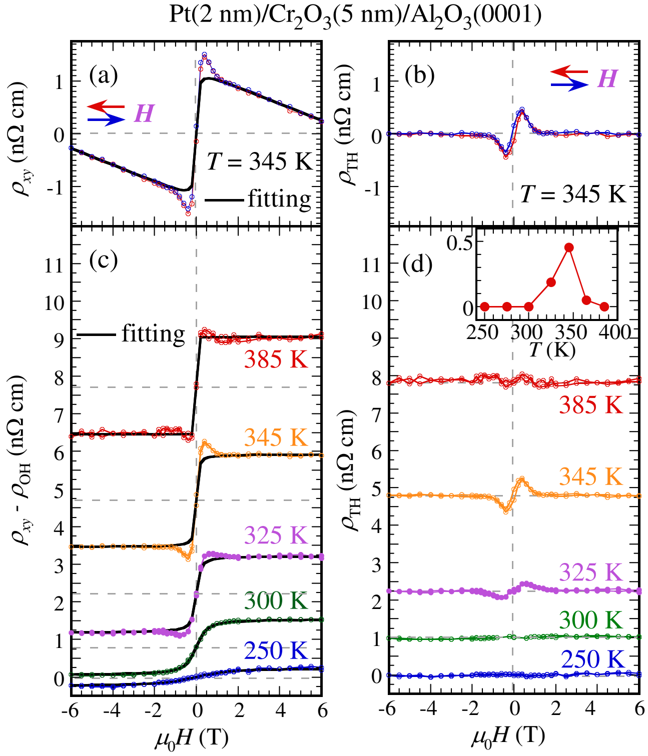

FIG. 2. Topological Hall (TH) measurements of a Pt (2 nm)/Cr_2O_3 (5 nm) bilayer on Al_2O_3 (0001). (a) Hall resistivity ρ_{xy} of Pt (2 nm)/Cr_2O_3 (5 nm)/Al_2O_3 (0001) at 345 K, where the black curve is the fitting for ρ_{AH} with the Langevin function and linear background due to ρ_{OH}. (b) TH resistivity after subtraction of the fitting curve for ρ_{AH} and ρ_{OH} in (a). (c) $\rho_{xy} - \rho_{\mathrm{OH}}$ at various temperatures from 250 to 385 K, where the black curves are the fitting for ρ_{AH} with the Langevin function. (d) ρ_{TH} after subtraction of the fitting curve for ρ_{AH} in (c) at each temperature. Inset: ρ_{TH} as a function of temperature.

upturn at $0.2\ \mathrm{T} < |H| < 1.4\ \mathrm{T}$ that cannot be explained by the SH AHE. We think it is very likely that the topological Hall effect (THE) leads to this upturn feature, which can be extracted by subtracting the ordinary Hall effect and SH AHE. The obtained ρ_{TH} vs H plot is presented in Fig. 2(b), which shows a TH region within $|H| < 1.4$ T with a peak value of 0.45 nΩ cm at ±0.4 T and sign switching at $H = 0$.

Following the same process, we measure ρ_{xy} of the Pt(2 nm)/Cr_2O_3(5 nm) bilayer on Al_2O_3(0001) from $T =$ 250 to 385 K and fit the data using the Langevin function, as shown in Fig. 2(c). Figure 2(d) shows the corresponding ρ_{TH} vs H plots and the inset gives the temperature dependence of ρ_{TH}, which indicate that ρ_{TH} disappears below 300 K and above 365 K. The observed THE in our Pt/Cr_2O_3 bilayer indicates spin chirality in the Cr_2O_3 film, which is attributed to the DMI at the Pt/Cr_2O_3 interface (for more details about the DMI at Pt/Cr_2O_3 interface, see the Supplemental Material [33]). The spin chirality at $T > T_C$ has been observed in FM $SrRuO_3$ and V-doped Sb_2Te_3 [23], which was explained as spin chirality fluctuations in quasi-two-dimensional FMs with weak DMI. Unlike the FMs where the THE appears within a small temperature window near and above T_C, the THE in the AF Cr_2O_3 films is robust even at 60 K above its bulk T_N.

We next conduct Hall measurement for various Cr_2O_3 thicknesses at 345 K, as shown in Figs. 3(a) and 3(b). The TH peaks persist at $t = 3$ to 5 nm and disappear at 6 nm. Besides, the ρ_{TH} peak position moves from 0.8 to 0.4 T as t increases from 3 to 5 nm [23]. Figure 3(c) shows the thickness dependence of ρ_{TH}, which drops suddenly to zero from 5 to 6 nm, indicating that the DMI is not large enough to stabilize spin textures in thicker Cr_2O_3 films [23]. Figure 3(e) summarizes the temperature-thickness phase diagram of ρ_{TH} for the Pt/Cr_2O_3 bilayers on Al_2O_3(0001).

To better understand the observed THE, we use Monte Carlo (MC) simulations to model the spin textures. Cr_2O_3 has a corundum structure and a rhombohedral unit cell. According to neutron measurements and first-principles calculations [34,35], the first and second-nearest neighbor exchange coupling constants J_1 and J_2 are dominant. Thus, the Hamiltonian can be written as

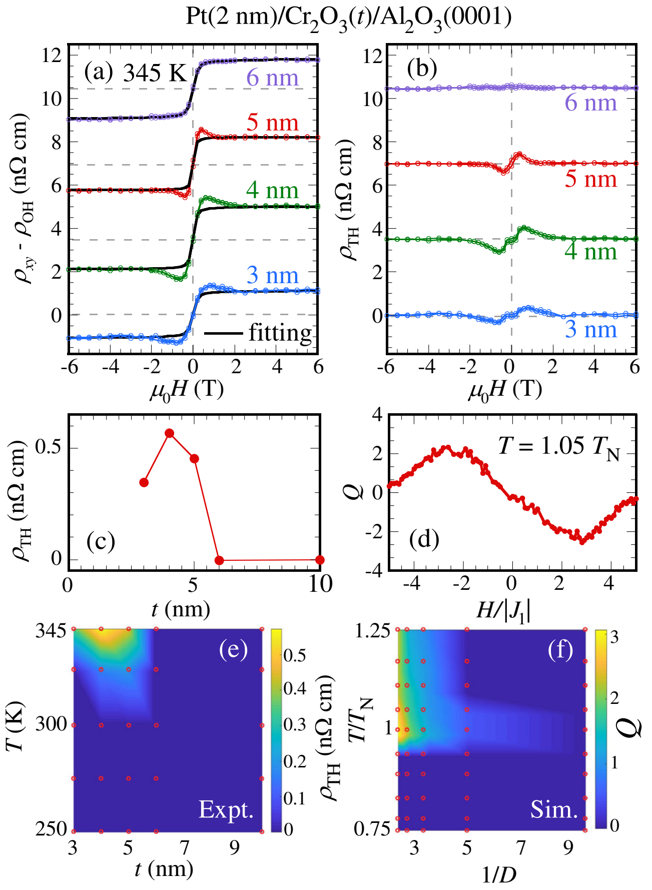

FIG. 3. (a) Hall resistivity $\rho_{xy} - \rho_{OH}$ of $Pt\,(2\ nm)/Cr_2O_3\,(t)$ bilayers on $Al_2O_3\,(0001)$ at 345 K with different thickness (t) of Cr_2O_3, where the black curves are the fitting for ρ_{AH} with the Langevin function. (b) ρ_{TH} of the bilayers after subtraction of the fitting curve in (a). (c) ρ_{TH} as a function of Cr_2O_3 thickness measured at 345 K. (d) Monte Carlo simulations of field dependence of topological charges Q at $T = 1.05\ T_N$ ($K = |J_1| = 1$ and $D = 0.5|J_1| = 0.5$ with out-of-plane easy axis anisotropy). (e) Contour plot of ρ_{TH} of $Pt\,(2\ nm)/Cr_2O_3\,(t)$ bilayers on $Al_2O_3\,(0001)$ as a function of temperature and Cr_2O_3 thickness. (f) Contour plot of topological charges Q as a function of temperature T/T_N and $1/D$ based on Monte Carlo simulation. The red circles in (e) and (f) are the data points.

$$H = -\sum_{\langle i,j\rangle} J_1(\boldsymbol{S_i}\cdot\boldsymbol{S_j}) - \sum_{\langle k,l\rangle} J_2(\boldsymbol{S_k}\cdot\boldsymbol{S_l}) + \sum_{\langle i,j\rangle} \boldsymbol{D_{ij}}\cdot(\boldsymbol{S_i}\times\boldsymbol{S_j}) - B_z\sum_i S_i^z - K\sum_i (S_i^z)^2, \tag{1}$$

where $\boldsymbol{S}$ is the unit spin vector, the third term is the DMI, the fourth term is the Zeeman energy, and the last term is the uniaxial anisotropy along $Cr_2O_3(0001)$. We choose $J_1 = -1$, $J_2 = -0.74$ based on first-principles calculations, and $K = 1$. D ranges from 0.1 to 0.5 to simulate DMI of different Cr_2O_3 thicknesses, which forbids spin chirality at low temperatures. We use six layers with 31×31 spins in each layer to rebuild the exchange coupling in the Cr_2O_3 rhombohedral unit cell along (0001) with the periodic boundary condition. The DMI is only exerted on the first layer and the spin chirality is indicated by the topological charge Q of the top layer [22]

$$Q = \frac{1}{4\pi}\int d^2\boldsymbol{r}\boldsymbol{S}\cdot(\partial_x\boldsymbol{S}\times\partial_y\boldsymbol{S}), \tag{2}$$

which can be calculated by the summation of the solid angle determined by three neighboring unit spin vectors in the first layer of spin lattice [36]. Figure 3(d) shows the field dependence of Q at $D = 0.5$ and $T = 1.05\ T_N$, where T_N is determined by the temperature dependence of susceptibility χ through MC simulation [37]. The antisymmetric curve of Q in Fig. 3(d) for Cr_2O_3 is similar to the reported simulations for FMs [23]. Since $\rho_{TH} \propto Q$, our simulations confirm the presence of spin chirality at $T > T_N$. Figure 3(f) summarizes the phase diagram of Q for $Cr_2O_3(0001)$ with varying T and $1/D$ ($D \propto 1/t$ for interfacial DMI [38]). The simulation captures the key features of the experimental data that spin chirality of $Cr_2O_3(0001)$ appears near and above T_N.

Cr_2O_3 is a uniaxial AF with spins aligned along the easy axis [0001]. To explore how the crystallographic and spin orientations affect the formation of spin textures, we perform the same measurements of ρ_{xy} for Pt/Cr_2O_3 bilayers grown on $Al_2O_3(11\bar{2}0)$ with an in-plane easy axis. Figure 4(a) shows the $\rho_{xy} - \rho_{OH}$ vs H data for a $Pt\,(2\ nm)/Cr_2O_3\,(5\ nm)$ bilayer on $Al_2O_3(11\bar{2}0)$ from

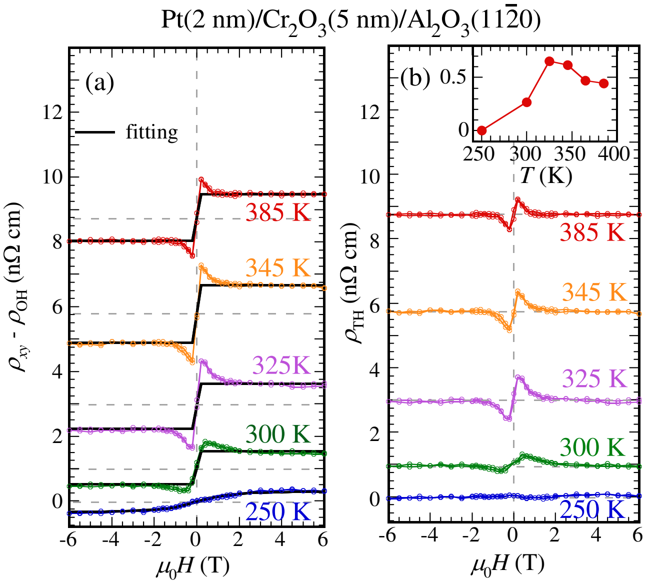

FIG. 4. (a) Hall resistivity $\rho_{xy} - \rho_{OH}$ of a $Pt\,(2\ nm)/Cr_2O_3$ (5 nm) bilayer on $Al_2O_3\,(11\bar{2}0)$ at various temperatures from 250 to 345 K, where the black curves are the fitting for ρ_{AH} with the Langevin function. (b) TH resistivity ρ_{TH} after subtraction of the fitting curve for ρ_{AH} in (a) at each temperature. Inset: ρ_{TH} as a function of temperature.

$T = 250$ to 385 K with a Langevin fitting for ρ_{AH}. The TH peaks are observed from 300 to 385 K, as compared to 325–365 K for Pt/$Cr_2O_3(0001)$. In addition, the TH peak appears at smaller fields, 0.2 T at 345 K as compared to 0.4 T for Pt/$Cr_2O_3(0001)$. Figure 4(b) shows the field dependence of ρ_{TH} obtained by subtracting the fitting curve of ρ_{AH} from $\rho_{xy} - \rho_{\mathrm{OH}}$. The magnitude of ρ_{TH} reaches the maximum at 325 K, as seen in the inset of Fig. 4(b). Surprisingly, there is a small nonzero TH signal even at 385 K. The differences in the TH signals between the bilayers grown on (0001)- and $(11\bar{2}0)$-orientated Al_2O_3 may be attributed to the different magnitude of uniaxial anisotropy and T_N due to strain [32,39], the direction of uniaxial anisotropy or spin configurations at the surface layer of Cr_2O_3. The detailed mechanism needs further exploration. However, we can conclude that the Pt/$Cr_2O_3(11\bar{2}0)$ bilayers share similar topological Hall features with the Pt/$Cr_2O_3(0001)$ bilayers.

Figure 5(a) shows the thickness dependence of $\rho_{xy} - \rho_{\mathrm{OH}}$ for Pt/$Cr_2O_3(t)$ bilayers on $Al_2O_3(11\bar{2}0)$ at 345 K, from which ρ_{TH} is extracted as shown in Fig. 5(b). The TH signal persists from 3 to 6 nm and vanishes at $t = 10$ nm. Meanwhile, the TH peak position is lowered from 0.6 to 0.2 T as t increases from 3 to 6 nm, which is similar to the Pt/$Cr_2O_3(0001)$ bilayers. The magnitude of ρ_{TH} has the maximum at 3 nm and then gradually decreases as Cr_2O_3 becomes thicker [Fig. 5(c)]. Figure 5(d) shows the MC simulation of topological charge Q in a varying out-of-plane field. For $Cr_2O_3(11\bar{2}0)$, we use four layers to rebuild the AF exchange coupling to the second-nearest neighbor. The last term in Eq. (1) is rewritten as $-K\sum_i (S_i^x)^2$ because of the in-plane easy axis. The similarity of Q between $Cr_2O_3(11\bar{2}0)$ and $Cr_2O_3(0001)$ is consistent with our experimental results. Compared with the $Cr_2O_3(0001)$ in Fig. 3(e), $Cr_2O_3(11\bar{2}0)$ has a broader $T - t$ range for THE as shown in Fig. 5(e). Figure 5(f) shows the simulation, which indicates a larger phase space of Q, possibly due to the different crystal orientation and anisotropy.

The similar phase diagrams of spin textures in the Cr_2O_3 films with different crystal and spin orientations indicate the minor role played by the uniaxial anisotropy. We believe the spin textures in our Pt/Cr_2O_3 bilayers have a similar fundamental origin as that in FM $SrRuO_3$ and V-doped Sb_2Te_3 [23]. The broken inversion symmetry at the Pt/Cr_2O_3 interface provides the DMI. Because of the relatively small DMI at Pt/Cr_2O_3 interface compared to the exchange interaction in Cr_2O_3 [40], spin textures can only emerge near or above T_N with the assistance of thermal fluctuations to overcome the strong AF exchange interaction. In conducting FM or AF layers that exhibit THE, conduction electrons are deflected by the emergent electromagnetic field due to the spin chirality. The proximity effect [41,42] in Pt/Cr_2O_3 bilayers is another possibility to explain the mapping of spin textures from Cr_2O_3 to Pt, while to date, the existence of proximity in Pt/Cr_2O_3 is debatable [42–44] and it is unlikely to preserve the moment in Pt at $T > T_N$ [45]. We propose a new mechanism, the spin Hall topological Hall effect (SH THE) [46,47], which is similar to the SH AHE in Pt/FMI and AFI bilayers. The SH THE arises from the following process. (1) As a current flows through the Pt layer, it generates spin accumulation via the spin Hall effect at the Pt/Cr_2O_3 interface. (2) The spin accumulation exerts a spin torque on the AF moments in Cr_2O_3, which form spin textures at appropriate thickness and temperature range. (3) The spins in Pt at the interface experience a reaction torque from the

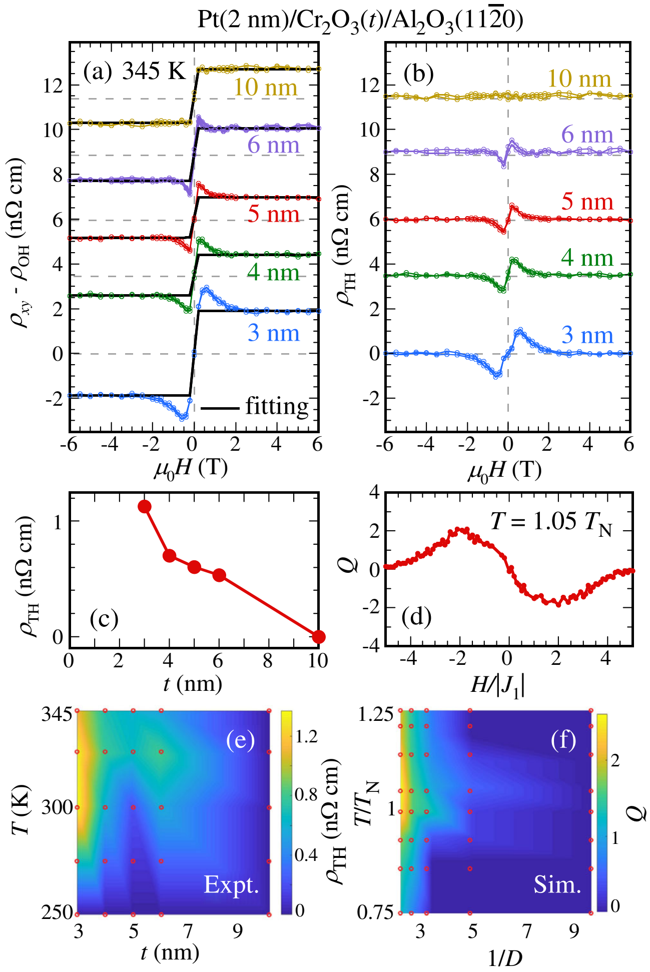

FIG. 5. (a) Hall resistivity $\rho_{xy} - \rho_{\mathrm{OH}}$ of Pt (2 nm)/Cr_2O_3 (t) bilayers on Al_2O_3 $(11\bar{2}0)$ at 345 K with different Cr_2O_3 thicknesses where the black curves are the fitting for ρ_{AH} with the Langevin function. (b) ρ_{TH} of the bilayers after subtraction of the fitting curve in (a). (c) ρ_{TH} as a function of Cr_2O_3 thickness measured at 345 K. (d) Monte Carlo simulations of field dependence of topological charges Q at $T = 1{:}05T_N$ ($K = |J_1| = 1$ and $D = 0.5$ $|J_1| = 0.5$ with easy in-plane anisotropy). (e) Contour plot of ρ_{TH} of Pt (2 nm)/Cr_2O_3 (t) bilayers on Al_2O_3 $(11\bar{2}0)$ as a function of temperature and Cr_2O_3 thickness. (f) Contour plot of topological charges Q as a function of temperature T/T_N and $1/D$ based on Monte Carlo simulation. The red circles in (e) and (f) are the data points.

winding AF spin textures in Cr_2O_3 and acquire a Berry phase, resulting in the topological Hall effect. This process should apply to both FMI and AFI based bilayers. Similar SH THE has also been observed in $Pt/Tm_3Fe_5O_{12}$ bilayers [47].

In summary, we observe strong evidence of the topological Hall effect in Pt/Cr_2O_3 bilayers at temperatures near or above the T_N, revealing the emergence of spin textures in collinear AF insulator films. This first evidence of the topological Hall effect in HM-AFI bilayers significantly expands our materials base to include the large family of AF insulators for the exploration of AF-based skyrmion technology.

This work was supported primarily by the U.S. Department of Energy (DOE) under Grant No. DE-SC0001304. Partial support is provided by DARPA under Grant No. D18AP00008 (structural characterization).

---

[*] Y. C. and S. Y. contributed equally to this work.

[1] N. Nagaosa and Y. Tokura, Topological properties and dynamics of magnetic skyrmions, Nat. Nanotechnol. **8**, 899 (2013).

[2] X. Z. Yu, N. Kanazawa, Y. Onose, K. Kimoto, W. Z. Zhang, S. Ishiwata, Y. Matsui, and Y. Tokura, Near room-temperature formation of a skyrmion crystal in thin-films of the helimagnet FeGe, Nat. Mater. **10**, 106 (2011).

[3] K. Shibata, X. Z. Yu, T. Hara, D. Morikawa, N. Kanazawa, K. Kimoto, S. Ishiwata, Y. Matsui, and Y. Tokura, Towards control of the size and helicity of skyrmions in helimagnetic alloys by spin-orbit coupling, Nat. Nanotechnol. **8**, 723 (2013).

[4] W. J. Jiang, P. Upadhyaya, W. Zhang, G. Q. Yu, M. B. Jungfleisch, F. Y. Fradin, J. E. Pearson, Y. Tserkovnyak, K. L. Wang, O. Heinonen, S. G. E. te Velthuis, and A. Hoffmann, Blowing magnetic skyrmion bubbles, Science **349**, 283 (2015).

[5] L. Vistoli, W. B. Wang, A. Sander, Q. X. Zhu, B. Casals, R. Cichelero, A. Barthélémy, S. Fusil, G. Herranz, S. Valencia, R. Abrudan, E. Weschke, K. Nakazawa, H. Kohno, J. Santamaria, W. D. Wu, V. Garcia, and M. Bibes, Giant topological Hall effect in correlated oxide thin films, Nat. Phys. **15**, 67 (2019).

[6] J. Matsuno, N. Ogawa, K. Yasuda, F. Kagawa, W. Koshibae, N. Nagaosa, Y. Tokura, and M. Kawasaki, Interface-driven topological Hall effect in $SrRuO_3$-$SrIrO_3$ bilayer, Sci. Adv. **2**, e1600304 (2016).

[7] J. C. Gallagher, K. Y. Meng, J. T. Brangham, H. L. Wang, B. D. Esser, D. W. McComb, and F. Y. Yang, Robust Zero-Field Skyrmion Formation in FeGe Epitaxial Thin Films, Phys. Rev. Lett. **118**, 027201 (2017).

[8] A. Neubauer, C. Pfleiderer, B. Binz, A. Rosch, R. Ritz, P. G. Niklowitz, and P. Boni, Topological Hall Effect in the A Phase of MnSi, Phys. Rev. Lett. **102**, 186602 (2009).

[9] N. Kanazawa, S. Seki, and Y. Tokura, Noncentrosymmetric magnets hosting magnetic skyrmions, Adv. Mater. **29**, 1603227 (2017).

[10] A. Fert, N. Reyren, and V. Cros, Magnetic skyrmions: Advances in physics and potential applications, Nat. Rev. Mater. **2**, 17031 (2017).

[11] Y. Taguchi, Y. Oohara, H. Yoshizawa, N. Nagaosa, and Y. Tokura, Spin chirality, berry phase, and anomalous Hall effect in a frustrated ferromagnet, Science **291**, 2573 (2001).

[12] T. Kampfrath, A. Sell, G. Klatt, A. Pashkin, S. Mahrlein, T. Dekorsy, M. Wolf, M. Fiebig, A. Leitenstorfer, and R. Huber, Coherent terahertz control of antiferromagnetic spin waves, Nat. Photonics **5**, 31 (2011).

[13] X. Marti, I. Fina, C. Frontera, J. Liu, P. Wadley, Q. He, R. J. Paull, J. D. Clarkson, J. Kudrnovsky, I. Turek, J. Kunes, D. Yi, J. H. Chu, C. T. Nelson, L. You, E. Arenholz, S. Salahuddin, J. Fontcuberta, T. Jungwirth, and R. Ramesh, Room-temperature antiferromagnetic memory resistor, Nat. Mater. **13**, 367 (2014).

[14] V. Baltz, A. Manchon, M. Tsoi, T. Moriyama, T. Ono, and Y. Tserkovnyak, Antiferromagnetic spintronics, Rev. Mod. Phys. **90**, 015005 (2018).

[15] C. A. Akosa, O. A. Tretiakov, G. Tatara, and A. Manchon, Theory of the Topological Spin Hall Effect in Antiferromagnetic Skyrmions: Impact on Current-Induced Motion, Phys. Rev. Lett. **121**, 097204 (2018).

[16] B. Göbel, A. Mook, J. Henk, and I. Mertig, Antiferromagnetic skyrmion crystals: Generation, topological Hall, and topological spin Hall effect, Phys. Rev. B **96**, 060406(R) (2017).

[17] X. C. Zhang, Y. Zhou, and M. Ezawa, Antiferromagnetic skyrmion: Stability, creation and manipulation, Sci. Rep. **6**, 24795 (2016).

[18] C. Sürgers, G. Fischer, P. Winkel, and H. v. Löhneysen, Large topological Hall effect in the noncollinear phase of an antiferromagnet, Nat. Commun. **5**, 3400 (2014).

[19] Q. L. He, G. Yin, L. Y. Yu, A. J. Grutter, L. Pan, C.-Z. Chen, X. Y. Che, G. Q. Yu, B. Zhang, Q. M. Shao, A. L. Stern, B. Casas, J. Xia, X. D. Han, B. J. Kirby, R. K. Lake, K. T. Law, and K. L. Wang, Topological Transitions Induced by Antiferromagnetism in a Thin-Film Topological Insulator, Phys. Rev. Lett. **121**, 096802 (2018).

[20] G. Q. Yu, A. Jenkins, X. Ma, S. A. Razavi, C. L. He, G. Yin, Q. M. Shao, Q. L. He, H. Wu, W. J. Li, W. J. Jiang, X. F. Han, X. Q. Li, A. C. Bleszynski Jayich, P. K. Amiri, and K. L. Wang, Room-temperature skyrmions in an antiferromagnet-based heterostructure, Nano Lett. **18**, 980 (2018).

[21] Y. L. Lu, X. Guo, V. Koval, and C. L. Jia, Topological thermal Hall effect driven by spin-chirality fluctuations in frustrated antiferromagnets, Phys. Rev. B **99**, 054409 (2019).

[22] W.-T. Hou, J.-X. Yu, M. Daly, and J. D. Zang, Thermally driven topology in chiral magnets, Phys. Rev. B **96**, 140403 (2017).

[23] W. B. Wang, M. W. Daniels, Z. L. Liao, Y. F. Zhao, J. Wang, G. Koster, G. Rijnders, C. Z. Chang, D. Xiao, and W. D. Wu, Universal spin chirality fluctuation in two-dimensional Ising ferromagnets, arXiv:1812.07005.

[24] A. J. Hauser, R. E. A. Williams, R. A. Ricciardo, A. Genc, M. Dixit, J. M. Lucy, P. M. Woodward, H. L. Fraser, and F. Y. Yang, Unlocking the potential of half-metallic Sr_2FeMoO_6 films through controlled stoichiometry and

double-perovskite ordering, Phys. Rev. B **83**, 014407 (2011).

[25] B. Peters, A. Alfonsov, C. G. F. Blum, S. J. Hageman, P. M. Woodward, S. Wurmehl, B. Büchner, and F. Y. Yang, Epitaxial films of Heusler compound $Co_2FeAl_{0.5}Si_{0.5}$ with high crystalline quality grown by off-axis sputtering, Appl. Phys. Lett. **103**, 162404 (2013).

[26] A. J. Lee, J. T. Brangham, Y. Cheng, S. P. White, W. T. Ruane, B. D. Esser, D. W. McComb, P. C. Hammel, and F. Y. Yang, Metallic ferromagnetic films with magnetic damping under 1.4×10^{-3}, Nat. Commun. **8**, 234 (2017).

[27] F. Y. Yang and P. C. Hammel, Topical review: FMR-driven spin pumping in $Y_3Fe_5O_{12}$-based structures, J. Phys. D **51**, 253001 (2018).

[28] S. X. Huang and C. L. Chien, Extended Skyrmion Phase in Epitaxial FeGe(111) Thin Films, Phys. Rev. Lett. **108**, 267201 (2012).

[29] Y. T. Chen, S. Takahashi, H. Nakayama, M. Althammer, S. T. B. Goennenwein, E. Saitoh, and G. E. W. Bauer, Theory of spin Hall magnetoresistance, Phys. Rev. B **87**, 144411 (2013).

[30] Y. Ji, J. Miao, Y. M. Zhu, K. K. Meng, X. G. Xu, J. K. Chen, Y. Wu, and Y. Jiang, Negative spin Hall magnetoresistance in antiferromagnetic Cr_2O_3/Ta bilayer at low temperature region, Appl. Phys. Lett. **112**, 232404 (2018).

[31] S. Foner, High-field antiferromagnetic resonance in Cr_2O_3, Phys. Rev. **130**, 183 (1963).

[32] T. Lino, T. Moriyama, H. Iwaki, H. Aono, Y. Shiratsuchi, and T. Ono, Resistive detection of the Néel temperature of Cr_2O_3 thin films, Appl. Phys. Lett. **114**, 022402 (2019).

[33] See Supplemental Material at http://link.aps.org/supplemental/10.1103/PhysRevLett.123.237206 for SQUID measurement, Hall measurements in control samples and a detailed comparison between experimental data and simulation.

[34] K. Lee, Y. Youn, and S. Han, Identification of ground-state spin ordering in antiferromagnetic transition metal oxides using the Ising model and a genetic algorithm, Sci. Technol. Adv. Mater. **18**, 246 (2017).

[35] E. J. Samuelsen, M. T. Hutchings, and G. Shirane, Inelastic neutron scattering investigation of spin waves and magnetic interactions in Cr_2O_3, Physica (Utrecht) **48**, 13 (1970).

[36] I. A. Iakovlev, O. M. Sotnikov, and V. V. Mazurenko, Supervised learning approach for recognizing magnetic skyrmion phases, Phys. Rev. B **98**, 174411 (2018).

[37] A. K. Murtazaev, Critical properties of the model of antiferromagnet Cr_2O_3, Low Temp. Phys. **25**, 344 (1999).

[38] J. Cho, N.-H. Kim, S. Lee, J.-S. Kim, R. Lavrijsen, A. Solignac, Y. X. Yin, D.-S. Han, N. J. J. van Hoof, H. J. M. Swagten, B. Koopmans, and C.-Y. You, Thickness dependence of the interfacial Dzyaloshinskii–Moriya interaction in inversion symmetry broken systems, Nat. Commun. **6**, 7635 (2015).

[39] Y. Kota, H. Imamura, and M. Sasaki, Strain-induced Néel temperature enhancement in corundum-type Cr_2O_3 and Fe_2O_3, Appl. Phys. Express **6**, 113007 (2013).

[40] A. Belabbes, G. Bihlmayer, F. Bechstedt, S. Blügel, and A. Manchon, Hund's Rule-Driven Dzyaloshinskii-Moriya Interaction at $3d-5d$ Interfaces, Phys. Rev. Lett. **117**, 247202 (2016).

[41] W. Amamou, I. V. Pinchuk, A. H. Trout, R. E. A. Williams, N. Antolin, A. Goad, D. J. O'Hara, A. S. Ahmed, W. Windl, D. W. McComb, and R. K. Kawakami, Magnetic proximity effect in $Pt/CoFe_2O_4$ bilayers, Phys. Rev. Mater. **2**, 011401 (2018).

[42] Y. Cheng, S. S. Yu, A. S. Ahmed, M. L. Zhu, J. Hwang, and F. Y. Yang, Anisotropic magnetoresistance and nontrivial spin magnetoresistance in $Pt/\alpha-Fe_2O_3$ bilayers: Evidence for antiferromagnetic proximity effect, arXiv:1906.04395.

[43] S. Seki, T. Ideue, M. Kubota, Y. Kozuka, R. Takagi, M. Nakamura, Y. Kaneko, M. Kawasaki, and Y. Tokura, Thermal Generation of Spin Current in an Antiferromagnet, Phys. Rev. Lett. **115**, 266601 (2015).

[44] N. Wu, X. He, A. L. Wysocki, U. Lanke, T. Komesu, K. D. Belashchenko, C. Binek, and P. A. Dowben, Imaging and Control of Surface Magnetization Domains in a Magnetoelectric Antiferromagnet, Phys. Rev. Lett. **106**, 087202 (2011).

[45] S. Cao, M. Street, J. Wang, J. Wang, X. Zhang, C. Binek, and P. A. Dowben, Magnetization at the interface of Cr_2O_3 and paramagnets with large stoner susceptibility, J. Phys. Condens. Matter **29**, 10LT01 (2017).

[46] Q. M. Shao, Y. W. Liu, G. Q. Yu, S. K. Kim, X. Y. Che, C. Tang, Q. L. He, Y. Tserkovnyak, J. Shi, and K. L. Wang, Topological Hall effect at above room temperature in heterostructures composed of a magnetic insulator and a heavy metal, National electronics review **2**, 182 (2019).

[47] A. S. Ahmed, A. J. Lee, N. Bagués, B. A. McCullian, A. M. A. Thabt, A. Perrine, J. R. Rowland, M. Randeria, P. C. Hammel, D. W. McComb, and F. Y. Yang, Spin-Hall topological Hall effect in highly tunable Pt/Ferrimagnetic-insulator bilayers, Nano Lett. **19**, 5683 (2019).